



Research article

Multiple Fano resonances on the metastructure of all-dielectric nanopore arrays excited by breaking two-different-dimensional symmetries

Liping Bi ^a, Xinye Fan ^{a,b,c,d,*}, Chuanchuan Li ^b, Hening Zhao ^a, Wenjing Fang ^{a,c,d,**}, Huijuan Niu ^{a,c,d}, Chenglin Bai ^{a,c,d}, Xin Wei ^{b,***}^a School of Physics Science and Information Engineering, Liaocheng University, Liaocheng, 252000, China^b Institute of Semiconductors, Chinese Academy of Sciences, Beijing, 100083, China^c Shandong Provincial Key Laboratory of Optical Communication Science and Technology, Liaocheng, 252000, China^d Liaocheng Key Laboratory of Industrial-Internet Research and Application, Liaocheng, 252000, China

ARTICLE INFO

Keywords:

All-dielectric

Metastructure

High Q-factor

BIC

Multiple Fano resonances

ABSTRACT

We have designed and analyzed the high quality-factor (Q-factor), multiple Fano resonances device on the basis of the all-dielectric metastructure. The unit structure consists of two rectangular air holes etched within a silicon cube and periodically aligns on the substrate of silicon dioxide. The results demonstrate that four Fano resonances are achieved by integrating the theory of bound states in the continuum (BIC) and breaking the symmetry (width symmetry or depth symmetry) of two rectangle air holes, and the resonant wavelength can be modified by altering structural parameters. The sensing characteristics of the presented structure are studied. The sensitivity (S) of 304 nm/RIU, the maximal Q-factor of 2142 and the figure of merit (FOM) of 515.3 are achieved while width symmetry is broken. Meanwhile, the sensitivity of 280 nm/RIU, the maximal Q-factor of 2517 and the FOM of 560 are got through breaking depth symmetry. The proposed metastructures can be used for the lasers, biosensing and nonlinear optics.

1. Introduction

Fano resonance has received a lot of attention for providing an effective way to achieve high Q-factors and suppress radiation losses, which are playing a significant part in the field of optoelectronics, such as nonlinear optics [1], biosensors [2], lasers [3], etc. The resonances are normally attributed to the interaction between a superradiant (highly radiative) mode and a subradiant (poorly radiative) mode, which can produce narrow resonance spectra to achieve high sensitivity [4-6]. The Fano resonance in some nanostructures of plasmonic based on metal materials have been observed, however, it is hard to get Fano resonances with high Q-factor due to ohmic losses [7-9]. The all-dielectric structure is characterised by low losses and is compatible to Complementary metal oxide semiconductor (CMOS) processes, as well as supporting the Fano resonance with high Q-factor [10]. In addition, recent studies have shown that toroidal dipole (TD) resonances in the all-dielectric metastructure can be stimulated [11,12], which is characterised by the

* Corresponding author. School of Physics Science and Information Engineering, Liaocheng University, Liaocheng, 252000, China.

** Corresponding author. School of Physics Science and Information Engineering, Liaocheng University, Liaocheng, 252000, China.

*** Corresponding author.

E-mail addresses: fanxinye@lcu.edu.cn (X. Fan), fangwenjing@lcu.edu.cn (W. Fang), weix@red.semi.ac.cn (X. Wei).<https://doi.org/10.1016/j.heliyon.2023.e12990>

Received 30 September 2022; Received in revised form 6 January 2023; Accepted 12 January 2023

Available online 16 January 2023

2405-8440/© 2023 The Authors. Published by Elsevier Ltd. This is an open access article under the CC BY-NC-ND license (<http://creativecommons.org/licenses/by-nc-nd/4.0/>).

flow of current over a toroidal surfaces or by the sequence of magnetic dipoles arranged along a closed pathway, and that Fano resonances with high Q-factors have been obtained by using low free space coupling [13,14]. Especially, non-radiative anapoles are produced when the TD resonance and the electric dipole (ED) resonance are superimposed at the identical scattering magnitude yet in different phase [15,16], and this can be employed for obtaining high Q-factor resonances. An effective method for realizing the Fano resonance of high Q-factor is based on bound states in the continuum (BIC) in all dielectric metastructure [17]. The ideal BIC is characterised by an exceptionally high Q-factor and an extremely thin linewidth. It is caused by an incompatibility from the mode's space symmetry to the external radiated wave's space symmetry. The ideal BIC is perturbed and switched into a quasi-BIC mode through the destruction of the symmetry that allows transmission into the external continuum, which leads to limitations on the linewidth and Q-factor of resonance. The research related to optical Fano resonance has expanded from mono-Fano resonance to multi-Fano resonances with the advancement of sensing technology [18-20].

Multiple Fano resonances can be used in a number of applications including multi-wavelength surface enhancement spectroscopy and multi-channel biosensors [21,22]. For example, Long et al. designed an all-dielectric metastructure composed by the couple with asymmetric nanorods for the realization of ultra-narrow-band Fano resonance [23]. Li et al. presented an all-dielectric metamaterial that breaks symmetry by varying the size of the semicircle radius, where TD-BIC can stimulate multiple Fano and display high Q-factor [24]. However, the multiple resonances are achieved by breaking only one-dimensional symmetry of the above structures.

In this paper, the multiple Fano resonances devices with high Q-factor based on the all-dielectric metastructure is presented. The proposed all-dielectric metastructure is composed by periodic silicon nanocubes with two rectangular air holes that are etched in the centre between the nanocubes and periodically lay out on the SiO₂ substrate in order to realize the TD response. The metastructure achieves multiple Fano resonances by breaking the width and depth symmetry, respectively. The metastructure I (MI) exhibit quasi-BIC of electric quadrupoles (EQ) resonance and magnetic dipole (MD) resonance through breaking width symmetry. The metastructure II (MII) displays quasi-BIC of TD resonance and MD resonance through breaking depth symmetry. High Q-factors are achieved for both metastructures. It's theoretically demonstrated that the maximum Q-factor of MI can achieve 2142, the S and FOM can reach 304 nm/RIU and 515.3, respectively. The maximum Q-factor of MII can achieve 2517, the S and FOM are 280 nm/RIU and 560, respectively. It is reasonable to believe that the presented metastructures can be used as the reference for medical, biosensor and non-linear optics applications.

2. Model and simulation

Fig. 1(a) demonstrates the unit cell of the MI is placed on a silicon dioxide substrate, which is composed of a silicon square with two rectangular air holes in the middle. The top view of a unit cell, as shown in Fig. 1(b). The width of two rectangle air holes are k_1 and k_2 , respectively, and L means the length of them. The asymmetry parameter $\Delta 1$ is defined as $\Delta 1 = k_2 - k_1$. The depth of the two air holes is H and the distance between them is expressed as d_1 . Fig. 2(a) shows the unit cell of the MII is composed by a square with two rectangular air holes of depth H and h in the middle being etched. Top view and side view of a unit cell, as shown in Fig. 2(b) and (c). The distance between the two stomata is denoted as d_2 , k_2 is the width of rectangle air holes and L denotes the length of them. The asymmetry parameter $\Delta 2$ is defined as $\Delta 2 = H - h$. The unit structural cycle is P_x and P_y along the x and y axes respectively and are set to $P_x = P_y = 760$ nm. Numerical simulation is conducted using the finite-difference time-domain (FDTD) solutions software. Both x and y directions are set as periodic boundary conditions and the perfectly matched layers (PML) can be used in the z-direction to absorb the incident wave energy. As shown in Figs. 1(a) and 2(a), there is an electric field polarised along the x-direction for a vertical incident plane wave whose vector of propagation lies in the z-direction. In addition, the mesh size of simulation area is set to 8 nm to ensure simulation precision. We have used the finite difference time domain method to analyze the transmission spectra and electromagnetic field distribution for the designed structures. Refractive indexes for both Si and SiO₂ materials can be found in the Palik Refractive Index database values [25].

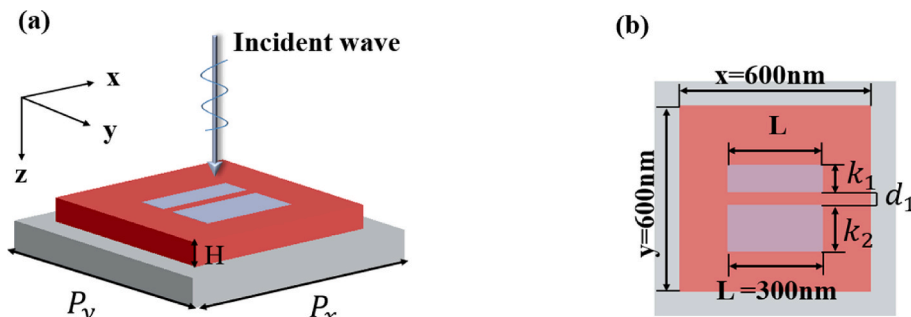


Fig. 1. Schematic diagram of the metastructure being proposed width-asymmetric MI. (a) The unit cell of the metastructure is placed on a silicon dioxide substrate and is composed of a silicon square with two rectangular air holes in the middle. (b) Top view of a unit cell, in which the geometrical parameters are set to $\Delta 1 = k_2 - k_1$, $x = y = 600$ nm, $P_x = P_y = 760$ nm, $d_1 = 40$ nm, and $H = 160$ nm. (For interpretation of the references to colour in this figure legend, the reader is referred to the Web version of this article.)

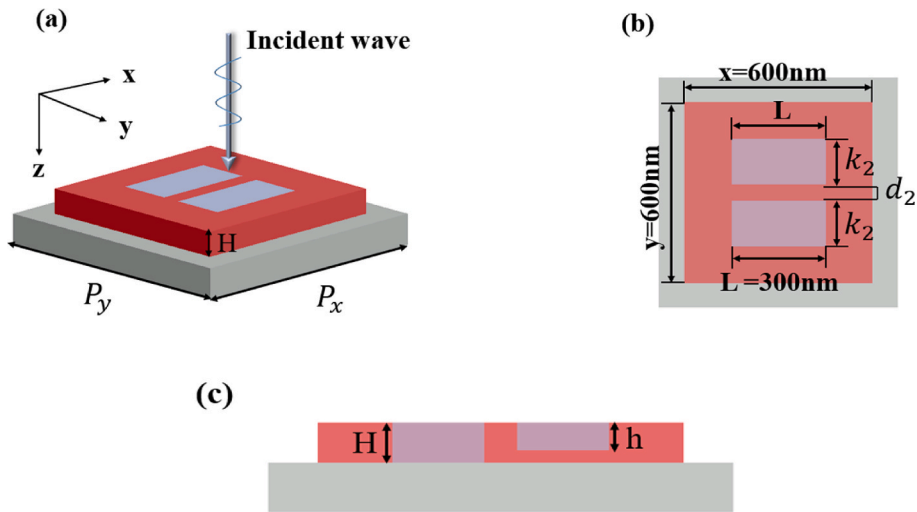


Fig. 2. Schematic diagram of the metastructure being proposed depth-asymmetric MII. (a) The unit cell of the metastructure is a nanocube with two rectangular pores etched in the middle with depths H and h respectively. (b)–(c) Top view and side view of a unit cell, in which the geometrical parameters are set to $\Delta 2 = H - h$, $x = y = 600 \text{ nm}$, $P_x = P_y = 760 \text{ nm}$, $d_2 = 55 \text{ nm}$, and $k_2 = 150 \text{ nm}$.

3. Results and discussion

The metastructure of different dimensions are analyzed by introducing symmetry breaking., where $\Delta 1$ and $\Delta 2$ are defined as the introduced width and depth asymmetry parameter, respectively. At $P_x = P_y = 760 \text{ nm}$, $x = y = 600 \text{ nm}$, $L = 300 \text{ nm}$, $H = 160 \text{ nm}$ and

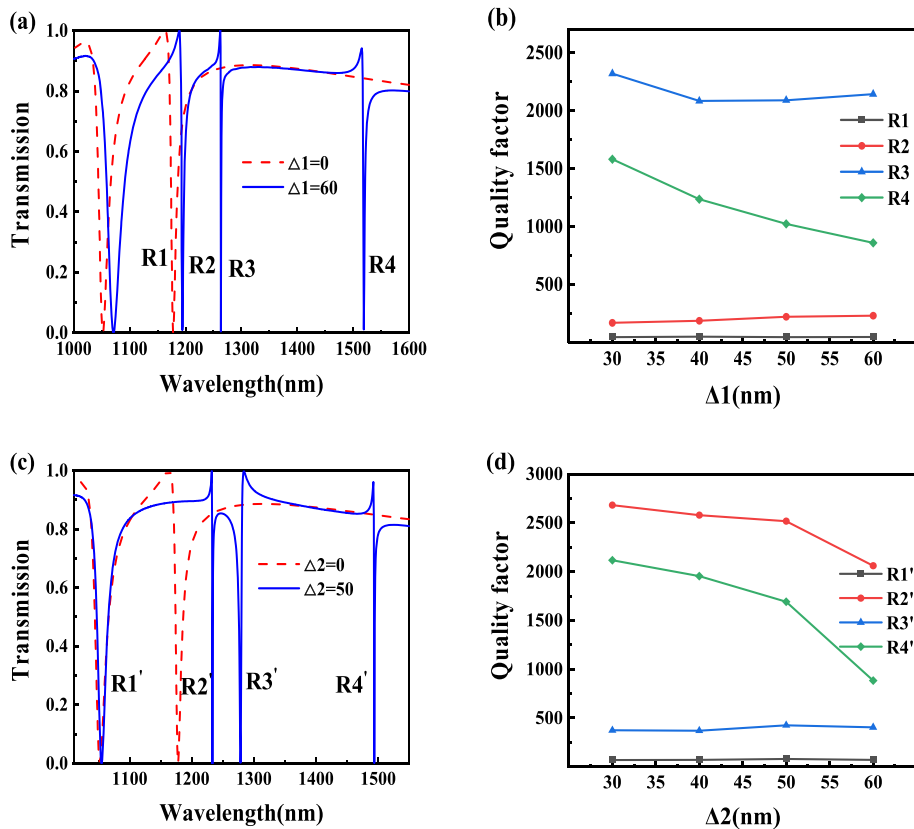


Fig. 3. Transmission spectra of the proposed structures at different symmetry parameters. (a) MI. (c) MII. The quality factors of the four resonance modes with different asymmetry parameters $\Delta 1$ and $\Delta 2$. (b) $\Delta 1$. (d) $\Delta 2$.

$d_1 = 40$ nm, the transmission spectra for metastructure breaking different symmetries are shown in Fig. 3. It can be seen that there are two Fano curves appear at $\lambda = 1052$ nm and $\lambda = 1177.7$ nm, respectively, arise while $k_1 = k_2 = 150$ nm, $H = h = 160$ nm ($\Delta_1 = 0$ nm, $\Delta_2 = 0$ nm). Due to the fact that the period of the metastructure (760 nm) is smaller compared to the operation wavelength, the structural symmetry breaking generates a zero-level radiation channel, which allows the BIC to leak and switch to the quasi-BIC mode. When breaking the width symmetry, i.e., $\Delta_1 = 60$ nm ($k_1 = 90$ nm, $k_2 = 150$ nm) or the etching depth symmetry, i.e., $\Delta_2 = 50$ nm ($H = 160$ nm, $h = 110$ nm), new Fano resonances are derived. The symmetry in the metastructure plane is disturbed by the difference between width or depth, thus, radiation channels are established among the free-space continuum and the non-radiative bound states that are available for identification and analysis according to the quasi-BIC model.

Fig. 3(a) shows the transmission spectra of MI with $\Delta_1 = 60$ nm ($k_1 = 90$ nm, $k_2 = 150$ nm). At $\lambda = 1263.2$ nm (R3) and $\lambda = 1518.8$ nm (R4), the new sharp Fano resonance peaks that correspond with the quasi-BIC model are excited. The initial two Fano resonance peaks displayed redshift at $\lambda = 1070.7$ nm (R1) and $\lambda = 1194$ nm (R2) respectively. The quasi-BIC mode of Fano resonance has finite but high Q-factor, which can strengthen the interactions between light and material in the structure. Consequently, the periodic all-dielectric metastructure can be analyzed for its transmission spectrum by means of the Fano model using the equation:

$$T(\omega) = \left| a_1 + ia_2 + \frac{b}{(\omega - \omega_0 + i\gamma)} \right|^2 \quad (1)$$

in which ω_0 is the resonant frequency and ω is the variable, a_1 , a_2 and b are defined as invariant real numbers, as well as γ being the damping rate of the structure. To calculate the Q-factors of the Fano resonances in the transmission spectra, simulated spectra can be fitted to Equation (1) and then they can be calculated by using Eq. (2):

$$Q = \frac{\omega_0}{2\gamma} \quad (2)$$

When the asymmetry parameter $\Delta_1 = 60$ nm, the Q-factors of R1, R2, R3 and R4 resonances can reach about 45, 299, 2142, 1022, respectively. The Q-factors change of the four resonance modes under different asymmetric parameter Δ_1 are shown in Fig. 3(b). Besides, it is evident that each of the four Fano resonances is characterised by a high modulation depth. The modulation depth (difference between the Fano peak and the Fano valley in the transmission spectra, i.e., $T_{peak} - T_{dip}$) at the R2 and R3 resonances can reach nearly 100%, as well as 91% and 92% at R1 and R4, respectively. Similarly, the transmission spectra of MII with $\Delta_2 = 50$ nm ($H = 160$ nm, $h = 110$ nm) is shown in Fig. 3(c). The new resonances at $\lambda = 1278.38$ nm (R3') and $\lambda = 1494.03$ nm (R4') appear in the transmission spectra that correspond to the quasi-BIC mode. The initial two Fano curves are red-shifted to $\lambda = 1054.5$ nm (R1') and $\lambda = 1233.2$ nm (R2'), respectively. The calculated Q-factors correspond to 81, 2517, 426, 1992, successively. Fig. 3(d) shows the Q-factors

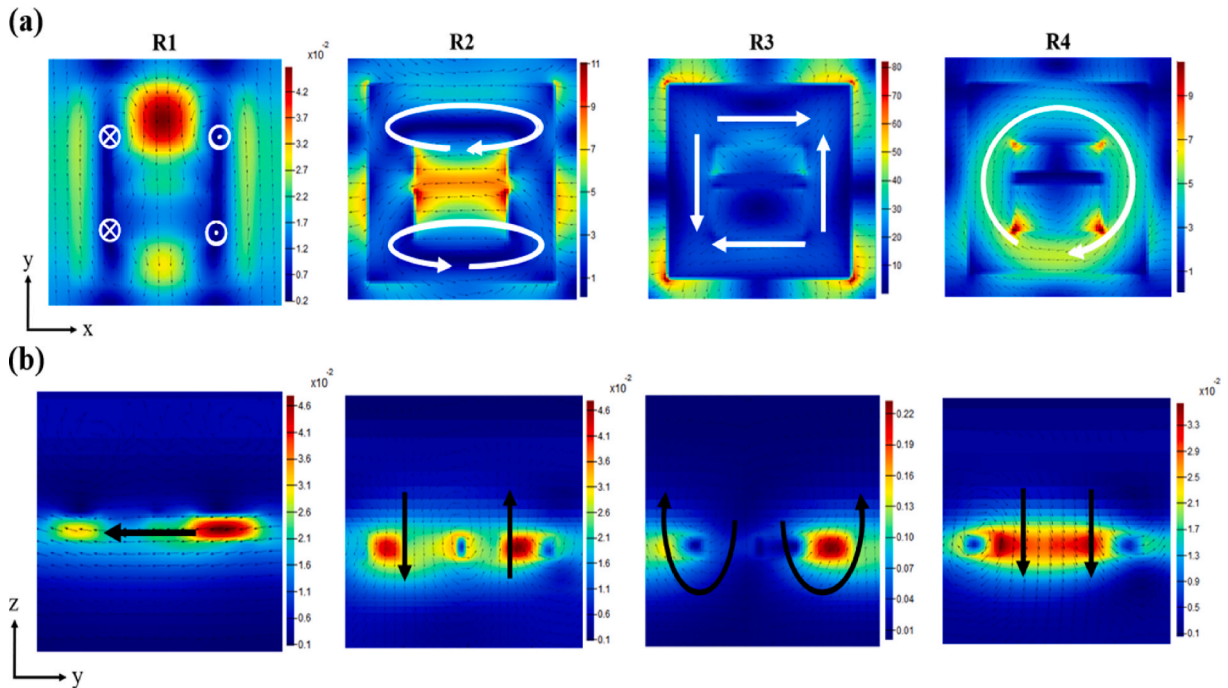


Fig. 4. When $\Delta_1 = 60$ nm, the near-field distribution of the normalized electric and magnetic fields corresponding to the four resonance peaks. (a) The coloured plots represent the distribution of E_z (H_z) at the location of the resonance peaks. Electric (magnetic) field vector distributions (small black arrows) and electric field directions (white arrows) at R2, R3 and R4 (R1) resonance modes. (b) The corresponding magnetic field amplitudes $|H/H_0|$ (coloured plots) and magnetic field directions (indicated by black arrows).

of the four resonance modes with different asymmetry parameter $\Delta 2$. The Fano resonance mode has nearly 100% modulation depth at $R2'$ and $R3'$, and the modulation depth at $R1'$ and $R4'$ also exceeds 91% and 97%, respectively. Hence, we can draw the conclusion that by breaking the symmetry in different dimensions of the metastructure multiple Fano resonances are excited, and that these resonance peaks have excellent performance indicators of high Q-factor and high modulation depth.

In order to visually analyze the Fano resonance, the near-field distributions of the electric and magnetic field inside a structure that breaks the symmetry of different dimensions and normalized to the incident electromagnetic field, as shown in Figs. 4 and 5. The electromagnetic field distributions of MI in the x - y plane and x - z plane at $\Delta 1 = 60$ nm are shown in Fig. 4(a) and (b), respectively. For the resonance mode at $R1$, the magnetic field creates two opposite circuits in the x-y plane and the magnetic field in the y-z plane is nearly a linear polarisation in the y direction, which results in MD resonance mode. In the $R2$ resonance mode, two electric field loops rotating on the x-y plane in contrary directions are presented, while the magnetic field on the y-z plane forms two opposite arrows and can form a complete loop, this can be recognized as a TD response in the x direction. In comparison to conventional electric dipoles (ED) and magnetic dipoles (MD), the TD response has a unique radiative characteristic which is a local electromagnetic excitation. At the $R3$ resonance mode, the distribution of the displacement current vector in the x - y plane presents an electric quadrupole (EQ) mode. The bright mode is characterized by dipole resonance, and the quadrupole resonance is a typical role as a dark mode feature. At the $R4$ resonant mode, a large current loop is formed in the x - y plane as well as a magnetic field oriented downwards in the y - z plane, so that the resonant mode is excited as MD and oscillates in the z direction. A more pronounced energy of the confined electric field can be observed in the gaps on both sides and around the structure.

The electromagnetic field distributions of MII in the x - y plane and x - z plane at $\Delta 1 = 60$ nm are shown in Fig. 5(a) and Fig. 5(b), respectively. For the resonant mode at $R1'$, where the magnetic field is formed in two opposite loops in the x-y plane and the two loops are oriented in the opposite orientation to that formed at $R1$, the linear polarisation of the magnetic field in the y-z plane is also oriented in the opposite direction to $R1$, which also leads to the MD resonant mode. In the $R2'$ resonance mode, the currents are reversed in the top and the bottom of the x - y plane, creating two vortex electric fields in the equal direction on the left and right sides. Meanwhile, two magnetic field reverse loops are formed in the y-z plane. Here, $R3'$ and $R4'$ are the same as the $R2$ and $R4$ resonance modes corresponding to the previously analyzed breaking of width symmetry, TD and MD, respectively. According to the above analysis we can conclude that not only can all new Fano resonance peaks be generated when different dimensional symmetries are broken, but the resonance peaks generated may also correspond to the same type of resonance.

To examine the effect of different variations of the geometrical parameters in the metastructure on the transmission spectra, we observed the transmission spectra for different variations of the geometrical parameters under the conditions at $\Delta 1 = 60$ nm and $\Delta 2 = 50$ nm, as shown in Figs. 6 and 7. All parameters are identical to those employed in Fig. 2, apart from the variable parameters indicated in each graph. The transmission spectra are distinct redshifted at the $R1$, $R3$ and $R4$ resonance peaks as the structure period changes from 750 nm to 770 nm, as illustrated in Fig. 6(a), while $R2$ generates a slight redshift. Fig. 6(b) displays the thickness of the silicon (i.

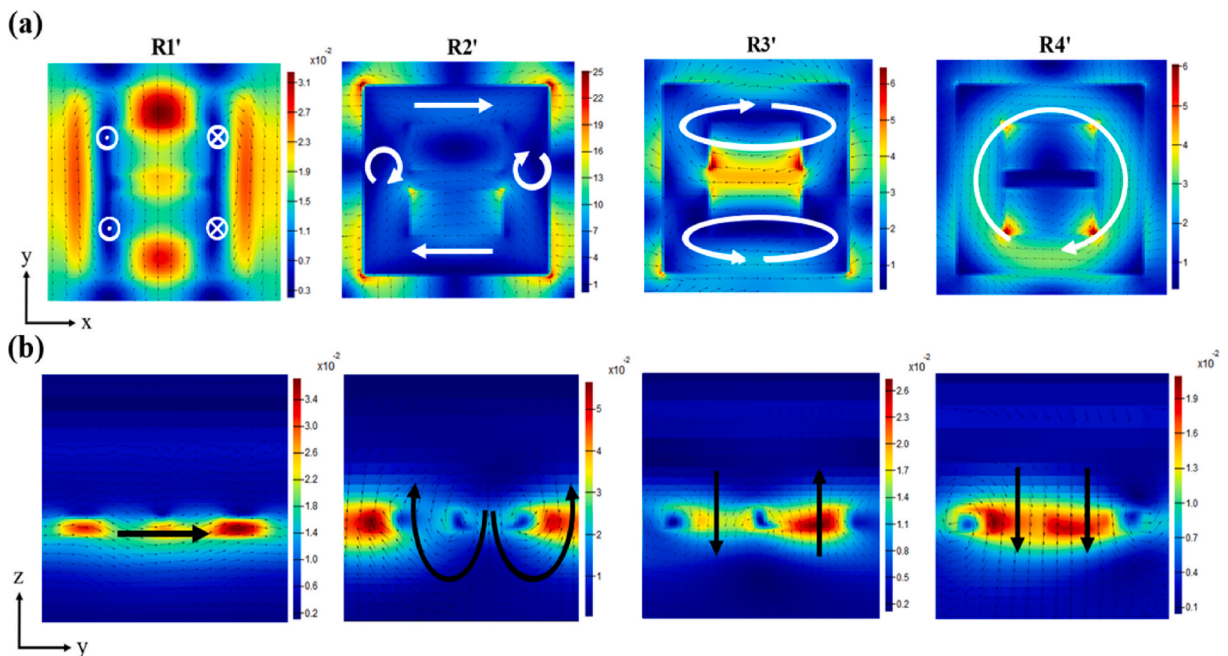


Fig. 5. When $\Delta 2 = 50$ nm, the near-field distribution of the normalized electric and magnetic fields corresponding to the four resonance peaks. (a) The coloured plots represent the distribution of E_z (H_x) at the location of the resonance peaks. Electric (magnetic) field vector distributions (small black arrows) and electric field directions (white arrows) at $R2'$, $R3'$ and $R4'$ ($R1'$) resonance modes. (b) The corresponding magnetic field amplitudes $|H/H_0|$ (coloured plots) and magnetic field directions (indicated by black arrows).

e., the etch depth of the rectangular hole) H increases to 165 nm from 155 nm and the transmission spectra are significantly redshifted at all resonance peaks, which is due to the effective refractive index of the structure MI contact increasing as a result of the increase in etch depth, but with minimal impact on the FWHM and Q-factor of the resonance peaks. It can be noticed that as the gap d_1 increases the shift of the R3 and R4 resonance peaks in the transmission spectra is hardly noticeable, as shown in Fig. 6(c), while the resonance peak R2 is found to be significantly redshifted it can be easily adjusted by the gap. As shown in Fig. 6(d), it is evident that all four Fano peaks are red-shifted when the asymmetry parameter $\Delta 1$ is increased to 70 nm from 50 nm. Simultaneously, the FWHM of the R1 and R4 resonance peaks widen with the increase in the asymmetry parameter, so that the Q-factors corresponding to the resonance peaks are significantly reduced.

Fig. 7(a) shows the transmittance spectra of the unit cell at different periods P . Simultaneously, it is observed that at the two resonant peaks of R3' and R4', the linewidths decrease slightly as the period P increases. As displayed in Fig. 7(b), as the width k_2 of the rectangle air holes increases to 155 nm from 145 nm, a clear blueshift is produced at four resonance peaks in the transmission spectra. Fig. 7(c) shows that the reduction in interactions with increasing gap d_2 can be found to result in a slight redshift of R2' and R3', while R4' experiences a significant blueshift. As shown in Fig. 7(d), it can be found that R1' and R2' are insensitive to the asymmetry parameter $\Delta 2$ and produce only a slight redshift, but both R3' and R4' undergo a significant redshift. Meanwhile, the linewidth of R3' and R4' become significantly wider as the asymmetry increases and the corresponding Q-factors are significantly lower.

The proposed metastructures can be used as a refractive index sensor for achieving high sensitivity because of its low radiation loss, high Q-factor and local field enhancement. Figs. 8 and 9 show the transmission spectra of the four resonance peaks when the MI and MII are covered by liquids with different refractive indexes. It is evident that a distinct shift in the location for the Fano resonance peak is achieved in spite of the minimal amount of change in refractive index. For the analysis of the sensing properties of the metastructure, the two key performance indicators S and FOM for sensing inspection can be calculated. Herein, $S = \Delta\lambda / \Delta n$ (nm/RIU), where $\Delta\lambda$ and Δn are the shift in wavelength corresponding to the resonance peak and the index of refraction change difference. Then the FOM is calculated by equation $FOM = S / FWHM$, which shows the sensitivity (S) to full width at half maximum (FWHM) ratio of the resonance peak. As shown in Fig. 8(a)-8(d), the transmission spectra exhibit clear redshifts in R1, R2, R3, and R4 resonance peaks when the MI is covered by the liquids with refractive index change from 1.02 to 1.08. Fig. 8(e) shows the wavelength shift of the four

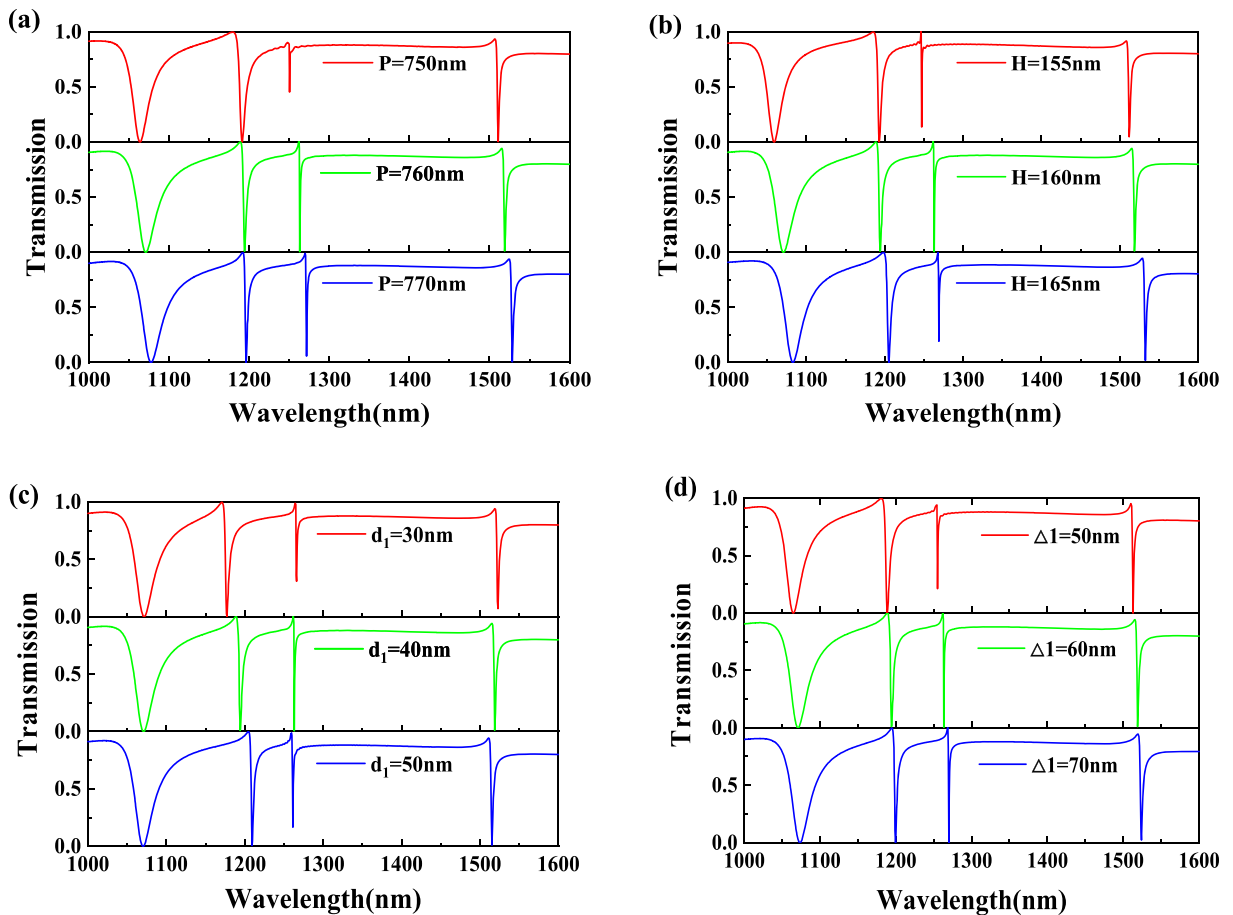


Fig. 6. Transmission spectra of MI for different parameters of the asymmetric array. (a) Different periods P , (b) Different etch depths H , (c) Different gaps d_1 and (d) Different asymmetry parameters $\Delta 1$.

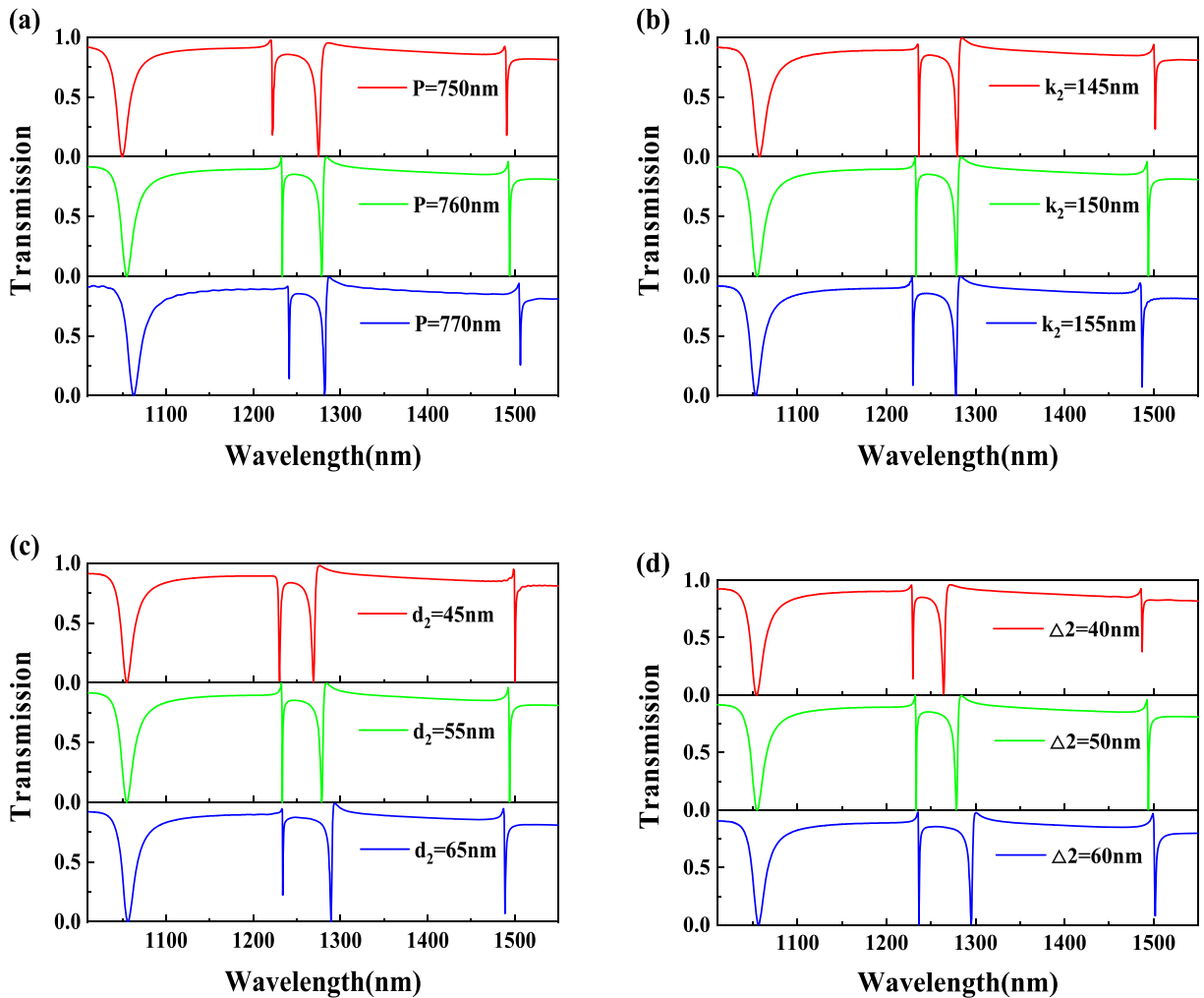


Fig. 7. Transmission spectra of MII for different parameters of the asymmetric array. (a) Different periods P , (b) Different width k_2 of the rectangle air holes, (c) Different gaps d_2 and (d) Different asymmetry parameters Δ_2 .

resonance peaks at different refractive indexes. The spectral shift sensitivity of R_1 , R_2 , R_3 , and R_4 resonances can reach about 127 nm/RIU, 170 nm/RIU, 304 nm/RIU, 100 nm/RIU, and the corresponding FOM reaches 22, 42.5, 515.3, and 67, respectively.

Fig. 9(a)-9(c) show the transmission spectra of R_1' , R_2' , R_3' and R_4' when the MII is covered by the liquids with the different refractive indexes. Fig. 9(d) shows the wavelength shift of the four resonance peaks of MII as the refractive index change from 1.02 to 1.08. Sensitivity of the R_1' , R_2' , R_3' and R_4' resonant modes are 120 nm/RIU, 280 nm/RIU, 180 nm/RIU, 80 nm/RIU, and the corresponding FOM reach 8.8, 560, 60, and 107, respectively. The variation of these Fano resonance sensitivities is due to the differences between the local field distributions.

The sensitivity and FOM calculated in this paper are compared with the corresponding values in the literature, as shown in Table 1, and it can be observed that the presented structure achieves high FOM and sensitivity. Breaking depth symmetry gives a narrower line width and a higher FOM, so it is considered that breaking depth symmetry alone is more suitable for sensing applications.

4. Conclusion

In summary, the proposed metastructures can generate four resonance peaks and produces different modes of resonance peaks by breaking different dimensional symmetries. The resonance modes from MI and MII are analyzed separately in the paper. The Q-factors of MI and MII can reach 2142 and 2517, respectively. In addition, the Q-factors of both are changed by tuning the asymmetric parameters of MI and MII. The S can reach 304nm/RIU and 280 nm/RIU, the FOM reach about 515.3 and 560, respectively. The proposed metastructures allow for the adjustment of the position of single or multiple resonance peaks by varying the parameters, which make them better suited to the application and to provide excellent optical performance indicators. The proposed sensor has extensive applications in multi-band bio-detection and non-linear optics as well as other opto-electronic devices.

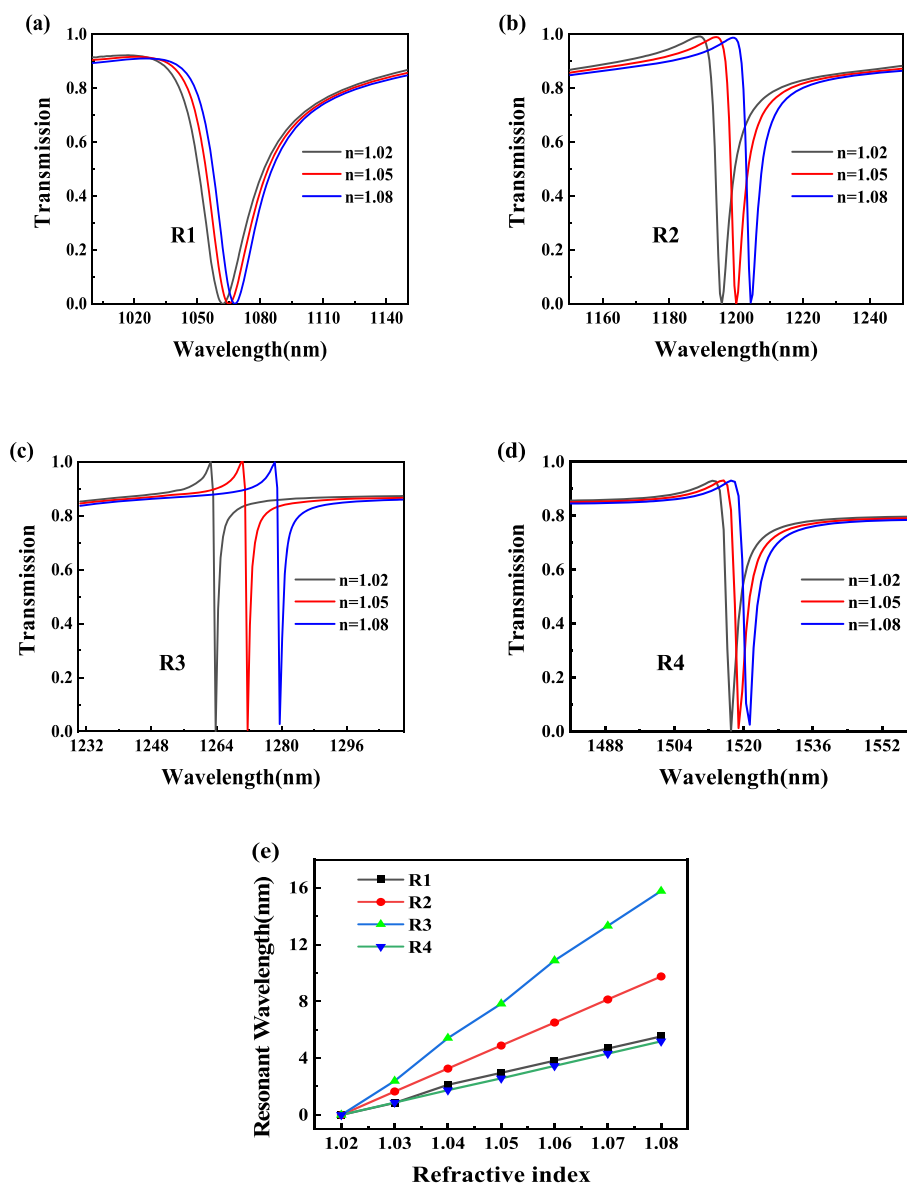


Fig. 8. (a)–(d) Transmission spectra of R1, R2, R3 and R4 when the MI is covered by the liquids with different refractive indexes, respectively. (e) The wavelength offset corresponding to the four resonance peaks as the refractive index changes from 1.02 to 1.08.

Author contribution statement

Liping Bi: Conceived and designed the experiments; Performed the experiments; Analyzed and interpreted the data; Wrote the paper.

Xinye Fan; Chuanchuan Li: Analyzed and interpreted the data; Contributed reagents, materials, analysis tools or data.

Hening Zhao: Performed the experiments.

Wenjing Fang: Conceived and designed the experiments; Analyzed and interpreted the data.

Huijuan Niu; Chenglin Bai: contributed reagents, materials, analysis tools or data.

Xin Wei: Performed the experiments; Contributed reagents, materials, analysis tools or data.

Funding statement

Mr Xinye Fan was supported by Natural Science Foundation of Shandong Province [ZR2021MF053], The 2021 Introduction and Education Plan for Young Scholars in Colleges and Universities of Shandong Province [2021RC085].

Wenjing Fang was supported by Natural Science Foundation of Shandong Province [ZR2021MF070], Open Fund of IPOC (BUPT)

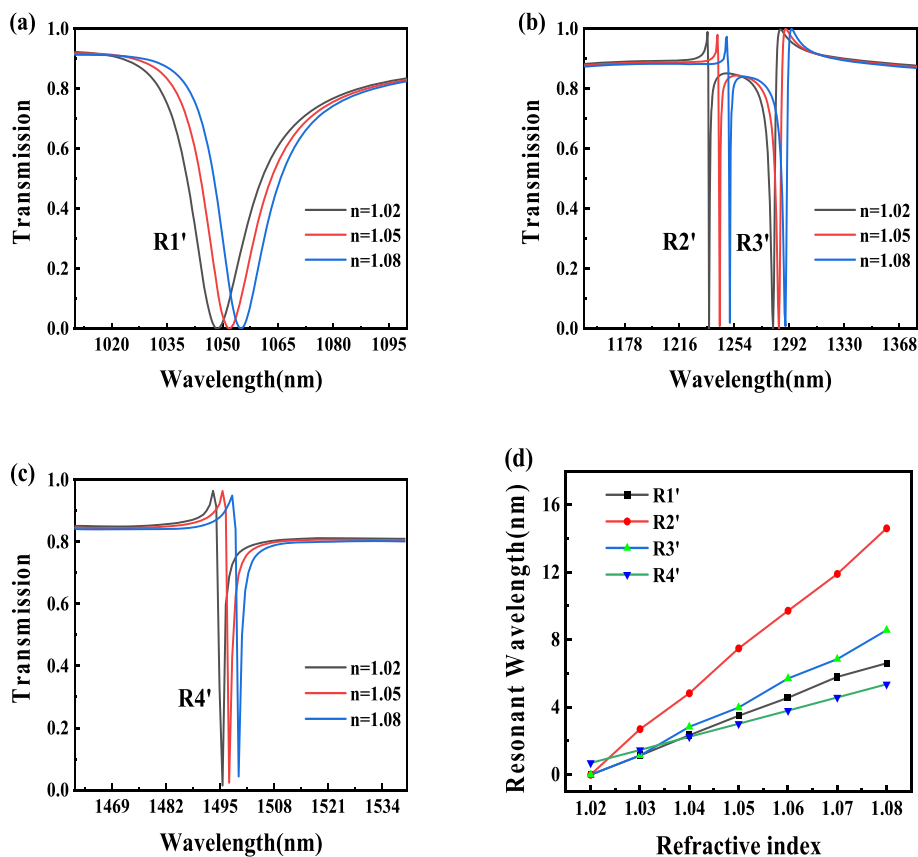


Fig. 9. (a)–(c) Transmission spectra of R1', R2', R3' and R4' when the MII is covered by the liquids with different refractive indexes, respectively. (d) The wavelength shifts corresponding to the four resonance peaks as the refractive index changes from 1.02 to 1.08.

Table 1

Comparison of sensitivity and FOM among different kinds in sensors.

Sensor Type	S (nm/RIU)	FOM (RIU ⁻¹)
Two-dimensional metal circular-hole [26]	1131	175
Double square hollow [27]	287.5	389
Semicircular holes [24]	300	440
Si split-ring [28]	452	56.5
U-shaped silicon cylinder [29]	203	29
MI	304	515.3
MII	280	560

[IPOC2019A009].

Huijuan Niu was supported by Open Fund of IPOC (BUPT) [IPOC2021B07], Doctoral Scientific Research Foundation of Liaocheng University [318052168], Natural Science Foundation of Shandong Province [ZR2022MF305].

Chenglin Bai was supported by Natural Science Foundation of Shandong Province [ZR2022MF253].

Data availability statement

Data will be made available on request.

Declaration of interest's statement

The authors declare no competing interests.

References

- [1] J. Butet, O.J. Martin, Fano resonances in the nonlinear optical response of coupled plasmonic nanostructures, *Opt Express* 22 (24) (2014) 29693–29707.
- [2] A.A. Siraji, Y. Zhao, High-sensitivity and high-Q-factor glass photonic crystal cavity and its applications as sensors, *Opt. Lett.* 40 (7) (2015) 1508–1511.
- [3] N.I. Zheludev, S.L. Prosvirnin, N. Papasimakis, V.A. Fedotov, Lasing spaser, *Nat. Photonics* 2 (6) (2008) 351–354.
- [4] A.E. Miroshnichenko, S. Flach, Y.S. Kivshar, Fano resonances in nanoscale structures, *Rev. Mod. Phys.* 82 (3) (2010) 2257.
- [5] B.W. Liu, X. Yao, L. Zhang, H.X. Lin, S. Chen, J.H. Zhong, B. Ren, Efficient platform for flexible engineering of superradiant, fano-type, and subradiant resonances, *ACS Photonics* 2 (12) (2015) 1725–1731.
- [6] S. Bakhti, N. Bonod, S.D. Dhuey, P.J. Schuck, N. Destouches, Fano-like resonance emerging from magnetic and electric plasmon mode coupling in small arrays of gold particles, *Sci. Rep.* 6 (1) (2016), 32061.
- [7] X. Wu, C. Dou, W. Xu, G. Zhang, R. Tian, H. Liu, Multiple Fano resonances in nanorod and nanoring hybrid nanostructures, *Chin. Phys. B* 28 (1) (2019) 431–436.
- [8] J.T. Liu, H.F. Hu, X.P. Shao, Polarization-insensitive ultra-narrow plasmon-induced transparency and short-range surface plasmon polariton Bloch wave in ultra-thin metallic film nanostructures, *Plasmonics* 14 (1) (2019) 139–146.
- [9] G. Dayal, X.Y. Chin, C. Soci, R. Singh, High-Q plasmonic Fano resonance for multiband surface-enhanced infrared absorption of molecular vibrational sensing, *Adv. Opt. Mater.* 5 (2) (2017), 1600559.
- [10] P. Genevet, F. Capasso, F. Aieta, M. Khorasaninejad, P. Genevet, R. Devlin, Recent advances in planar optics: from plasmonic to dielectric metasurfaces, *Optica* 4 (1) (2017) 139–152.
- [11] Y. Zhang, W. Liu, Z. Li, L. Zhi, H. Cheng, S. Chen, J. Tian, High-quality-factor multiple Fano resonances for refractive index sensing, *Opt. Lett.* 43 (8) (2018) 1842–1845.
- [12] X. Luo, X. Li, T. Lang, X. Jing, H. Zhi, Excitation of high Q toroidal dipole resonance in an all-dielectric metasurface, *Opt. Mater. Express* 10 (2) (2020) 358–368.
- [13] V.R. Tuz, V.V. Khardikov, Y.S. Kivshar, All-dielectric resonant metasurface with a strong toroidal response, *ACS Photonics* 5 (5) (2018) 1871–1876.
- [14] S.Q. Li, K.B. Crozier, Origin of the anapole condition as revealed by a simple expansion beyond the toroidal multipole, *Phys. Rev. B* 97 (24) (2018), 245423.
- [15] A.E. Miroshnichenko, A.B. Evlyukhin, Y.F. Yu, R.M. Bakker, A. Hipouline, A.I. uznetsov, B. Lukyanchuk, B.N. Chichkov, S. Kivshar, Nonradiating anapole modes in dielectric nanoparticles, *Nat. Commun.* 6 (1) (2015) 1–8.
- [16] L. Wei, Z. Xi, N. Bhattacharya, H.P. Urbach, Excitation of the radiationless anapole mode, *Optica* 3 (8) (2016) 799–802.
- [17] L. Yang, S.L. Yu, H. Li, T. Zhao, Multiple Fano resonances excitation on all-dielectric nanohole arrays metasurfaces, *Opt Express* 29 (10) (2021) 14905–14916.
- [18] R. Adhikari, D. Chauhan, R.K. Saini, S.H. Chang, R.P. Dwivedi, Subwavelength plasmonic liquid sensor using Fano resonance in a ring resonator structure, *Optik* 223 (2020), 165545.
- [19] W. Su, Y. Ding, Y. Luo, Y. Liu, A high figure of merit refractive index sensor based on Fano resonance in all-dielectric metasurface, *Results Phys.* 16 (2020), 102833.
- [20] S. Yu, Y. Wang, Z. Gao, H. Li, S. Song, J. Yu, T. Zhao, Dual-band polarization-insensitive toroidal dipole quasi-bound states in the continuum in a permittivity-asymmetric all-dielectric meta-surface, *Opt Express* 30 (3) (2022) 4084–4095.
- [21] S. Campione, S. Liu, L.I. Basilio, L.K. Warne, W.L. Langston, T.S. Luk, J.R. Wendt, J.L. Reno, G.A. Keeler, I. Brener, M.B. Sinclair, Broken symmetry dielectric resonators for high quality factor Fano metasurfaces, *ACS Photonics* 3 (12) (2016) 2362–2367.
- [22] Y. Zhang, W. Liu, Z. Li, Z. Li, H. Cheng, S. Chen, J. Tian, High-quality-factor multiple Fano resonances for refractive index sensing, *Opt. Lett.* 43 (8) (2018) 1842–1845.
- [23] X. Long, M. Zhang, Z. Xie, M. Tang, L. Li, Sharp Fano resonance induced by all-dielectric asymmetric metasurface, *Opt Commun.* 459 (2020), 124942.
- [24] S. Yu, H. Li, Y. Wang, Z. Gao, T. Zhao, J. Yu, Multiple Fano resonance excitation of all-dielectric nanoholes cuboid arrays in near infrared region, *Results Phys.* 28 (2021), 104569.
- [25] A.D.F. Edwards, in: E.D. Palik (Ed.), *Silicon (Si), Handbook of Optical Constants of Solids*, Academic, 1985.
- [26] J. Yu, J. Zhu, S. Ye, X. Wang, Ultra-wide sensing range plasmonic refractive index sensor based on a two-dimensional circular-hole grating engraved on a gold film, *Results Phys.* 26 (2021), 104396.
- [27] H. Li, S. Yu, L. Yang, T. Zhao, High Q-factor multi-Fano resonances in all-dielectric double square hollow metamaterials, *Opt Laser. Technol.* 140 (2021), 107072.
- [28] G. Liu, X. Zhai, L. Wang, Q. Lin, S. Xia, X. Luo, C. Zhao, A high-performance refractive index sensor based on Fano resonance in Si split-ring metasurface, *Plasmonics* 13 (1) (2018) 15–19.
- [29] M. Qin, C. Pan, Y. Chen, Q. Ma, S. Liu, E. Wu, B. Wu, Electromagnetically induced transparency in all-dielectric U-shaped Silicon metamaterials, *Appl. Sci.* 8 (10) (2018) 1799.